

1 **Effect of the Inhomogeneity of Ice Crystals on Retrieving Ice Cloud Optical**
2 **Thickness and Effective Particle Size**

3
4
5 **Yu Xie* and Ping Yang**

6 Department of Atmospheric Sciences, Texas A&M University, College Station, TX 77843

7
8 **George W. Kattawar**

9 Department of Physics, Texas A&M University, College Station, TX 77843

10
11 **Patrick Minnis and Yong X. Hu**

12 NASA Langley Research Center, Hampton, VA 23681

13
14
15
16
17 For publication in the
18 ***Journal of Geophysical Research***
19

20
21

22 * *Corresponding author address:* Yu Xie, Department of Atmospheric Sciences,
23 Texas A&M University, College Station, TX 77843; Tel: 979-458-0544
24 Email: xieyu@ariel.met.tamu.edu

Abstract

Spherical or spheroidal air bubbles are often trapped in rapidly growing ice crystals. In this study the single-scattering properties of inhomogeneous ice crystals containing air bubbles are investigated. Specifically, a combination of the ray-tracing technique and the Monte Carlo method is used to simulate the scattering of light by randomly oriented large hexagonal ice crystals containing spherical or spheroidal air bubbles. The effect of the air bubbles within ice crystals is to smooth the phase functions, diminish the 22° and 46° halo peaks, and reduce the backscatter in comparison with the case of bubble-free ice crystals. These features vary with the number, sizes, locations, and shapes of the air bubbles within the ice crystals. Moreover, the asymmetry factors of inhomogeneous ice crystals decrease as the ratio of air-bubble volume to ice crystal volume increases. Cloud reflectance look-up tables were generated at the wavelengths of $0.65\text{ }\mu\text{m}$ and $2.13\text{ }\mu\text{m}$ to examine the impact of accounting for air bubbles in ice crystal morphology on the retrieval of ice cloud optical thickness and effective particle size. The reflectances simulated for inhomogeneous ice crystals are larger than those computed for homogeneous ice crystals at a wavelength of $0.65\text{ }\mu\text{m}$. Thus, the retrieved cloud optical thickness is reduced by employing inhomogeneous ice cloud models. At a wavelength of $2.13\text{ }\mu\text{m}$, including air bubbles in ice crystal morphology may also increase the reflectance. This effect implies, particularly in the case of large air bubbles, that the retrieved effective particle size for inhomogeneous ice crystals is larger than that retrieved for homogeneous ice crystals,.

1. Introduction

An appropriate representation of ice clouds in radiative transfer simulations has long been a subject of great interest, not only because of their importance for cloud radiative forcing and the energy budget of the earth, but also because of the uncertainties associated with the shapes and sizes of ice crystals within these clouds [Ramanathan *et al.*, 1983; Liou, 1986; Baran, 2004]. Although approximating the single-scattering properties (e.g., phase function, single-scattering albedo and asymmetry factor) of realistic ice crystals by assuming one idealized geometrical shape is an oversimplification [Baum *et al.*, 2005a,b], it is significantly better for retrieving ice cloud properties than assuming that the clouds are composed of spherical ice crystals [Minnis *et al.*, 1993]. However, a more accurate representation of cirrus cloud ice crystal properties is needed. For example, the use of homogeneous hexagonal ice crystals [Minnis *et al.*, 1998] can yield accurate estimates of ice water path [Mace *et al.*, 2005], but the retrieved optical depth values tend to be low [Min *et al.*, 2004] implying an overestimate of the effective particle size. To further improve the representation of cloud ice crystals in radiative transfer calculations, steady progress has been made toward single-scattering computations involving various complex particle shapes.

Liou [1972] first assumed nonspherical ice crystals to be long circular cylinders, and demonstrated the significant differences in the phase functions between polydisperse spheres and equivalent long circular cylinders. Takano and Liou [1989], Muinonen [1989], Hess and Wiegner [1994], Borovoi and Grishin [2003] and many others applied the traditional ray-tracing method or its modified forms to the scattering of radiation by randomly and horizontally oriented hexagonal particles. The optical properties of various complicated ice crystals have also been simulated from the geometric optics method by

71 *Hess et al.* [1998], *Macke* [1993], *Macke et al.* [1996], *Iaquinta et al.* [1995], *Takano and*
72 *Liou* [1995], *Yang and Liou* [1998], *Baran and Labonnote* [2006, 2007], *Um and*
73 *McFarquhar* [2007], *Schmitt et al.* [2006], and *Yang et al.* [2008 a, b, c]. Furthermore,
74 *Yang and Liou* [1996] employed the finite-difference time domain (FDTD) method to
75 simulate the scattering of light by small bullet-rosettes, hexagonal plates, solid columns,
76 and hollow columns.

77 In the previously reported studies on the single-scattering properties of irregular
78 ice particles, homogeneous ice crystal morphologies were usually assumed. In the
79 accretion and aggregation of ice crystals, an ice particle may collide with supercooled
80 water droplets or other ice particles. When this happens, ice crystals can rapidly grow to
81 form large ice crystals. The collision and coalescence processes may lead to the trapping
82 of spherical or spheroidal air bubbles within ice crystals when the supercooled water
83 droplets freeze almost instantly. Air bubbles may be incorporated when water containing
84 dissolved air freezes into ice crystals. Supercooled water drops may turn into ice [*Hallett*,
85 1964]. The freezing process starts at the particle surface and slowly proceeds inward.
86 This inward growth of the ice may cause the previously dissolved air to be released and
87 subsequently form small bubbles within the ice particle. The size and concentration of air
88 bubbles are then influenced by the rate of freezing, amount of dissolved air in water and
89 temperature during the freezing process [*Carte*, 1961; *Hallett*, 1964].

90 There are only a handful of published studies on the optical properties of
91 inhomogeneous ice crystals because of the lack of laboratory and in situ measurements as
92 well as difficulties in specifying the shapes of air bubbles and other inclusions. Among
93 these previous studies, *Macke et al.* [1996] employed a combination of the ray-tracing

94 technique and the Monte Carlo method to investigate the single-scattering properties of
95 randomly oriented hexagonal ice columns containing ammonium sulfate inclusions, air
96 bubbles and soot impurities. In their computations, the scattering events at the outer
97 boundary of a hexagonal particle are considered by using the ray-tracing technique
98 [Macke, 1993], whereas the Monte Carlo method is used to account for the ray-path
99 changes due to the internal inclusions. Yang *et al.* [2000] used the FDTD technique to
100 compute the scattering phase functions of small ice crystals with inclusions of soot
101 impurities and air bubbles. Labonnote *et al.* [2001] developed an Inhomogeneous
102 Hexagonal Monocrystals (IHM) model for ice crystals containing randomly located air
103 bubbles and mineral aerosols. This single-scattering property model, based on the ray-
104 tracing and Monte Carlo techniques developed by Macke *et al.* [1996], has further
105 defined the internal air bubbles in terms of spherical voids with a size distribution.
106 Labonnote *et al.* [2001] and Knap *et al.* [2005] used the IHM model to investigate the
107 bulk-scattering properties of ice clouds and to compare the simulations with satellite-
108 based measurements of polarized radiances.

109 The IHM model does not account for the case where an ice crystal contains only a
110 few air bubbles with specific locations. The geometries of air bubbles in the previous
111 studies were restricted to the assumption of spheres, a constraint that is not always
112 realistic. This paper reports on a new inhomogeneous ice crystal model based on the
113 surface observations reported by Tape [1994]. Furthermore, the effects of the air bubbles
114 on the retrieval of cloud optical thickness and effective particle sizes are also
115 investigated. This paper is organized as follows. In Section 2, we describe the
116 morphologies of ice crystals observed by Tape [1994] and define the geometries of the

inhomogeneous ice crystals for the present scattering computations. Then, we introduce the single-scattering model based on an improved geometrical-optics method (IGOM, *Yang and Liou*, 1996). In Section 3, we illustrate the effect of the number, shape, size, and location of the air bubbles inside hexagonal ice crystals on the single-scattering properties of these particles. In Section 4, we demonstrate the effects of accounting for air bubbles in defining ice crystal morphology on the retrieval of ice cloud optical thickness and effective particle size. Moreover, we derive cloud microphysical and optical properties based on the Moderate Resolution Imaging Spectroradiometer (MODIS) measurements from a bi-spectral method originally developed by *Nakajima and King* [1990] and compare the retrieval results from homogeneous and inhomogeneous ice crystal models. The conclusions and discussions of this study are given in Section 5.

2. Single-scattering model for inhomogeneous ice crystals

Although the geometries of ice crystals in the atmosphere have been extensively studied on the basis of airborne in situ observations [*Korolev and Isaac*, 1999; *Heymsfield and Platt*, 1984; *McFarquhar and Heymsfield*, 1996], ground-based observations also provide useful data for investigating ice crystal morphologies. *Tape* [1983, 1994] used Petri dishes containing hexane or silicone oil and acrylic spray to collect ice crystals falling near the surface and observed the ice crystal shapes using a binocular microscope. Figure 1 illustrates the ice crystals sampled by *Tape* [1994] at the South Pole on January 19, 1985 and on January 17, 1986. In the photographs, the ice crystals have typical hexagonal shapes and most of these particles are inhomogeneous with embedded air bubbles. The observed inhomogeneous ice crystals spurred

development of the theoretical models used by *Macke et al.* [1993] and *Labonnote et al.* [2001] to compute the single-scattering properties of these particles. However, unlike the crystal geometries in the IHM model [*Labonnote et al.* 2001], an inhomogeneous ice crystal usually contains a few air bubbles with visible dimensions. The sizes of the air bubbles are relatively large, as the maximum dimensions of the air bubbles are comparable with the width of the ice crystal. Another significant difference between the observations by *Tape* [1994] and the IHM model is that the actual air bubbles are not always spheres, although most of them have spherical shapes. Moreover, the air bubbles are located almost exclusively along the symmetry axes of hexagonal columns. However, for hexagonal plates, more than one air bubble can be horizontally aligned near the surface of the particles.

Based on the ice particles photographed by *Tape* [1994], the geometries of inhomogeneous ice crystals in this study are defined as those shown in Fig. 2. For hexagonal columns, only one or two air bubbles are included within ice particles. Furthermore, the air bubble inclusions in our model are all on the axes of ice crystals (see the upper and middle panels in Fig. 2). For hexagonal plates, the air bubbles are aligned horizontally if more than one air bubble is included (see the lower panels in Fig. 2). The orientations of ice crystals for either hexagonal columns or plates are specified in the OXYZ coordinate system denoted in Fig. 3. Following *Yang and Liou* [1996], the Y-axis in Fig. 3 is perpendicular to one of the ice crystal's side faces, and the Z-axis is along the vertical axis of the hexagon. The shape of an air bubble is defined in terms of the following equation:

$$\frac{(x - x_r)^2}{r_1^2} + \frac{(y - y_r)^2}{r_2^2} + \frac{(z - z_r)^2}{r_3^2} = 1, \quad (1)$$

where r_1 , r_2 , and r_3 are the three semi-axes along the X, Y and Z axes, respectively, and the coordinates (x_r, y_r, z_r) specify the center of the air bubble in the OXYZ system.

In this study, the IGOM developed by *Yang and Liou*, [1996] is used to compute the single-scattering properties of inhomogeneous ice crystals. At the outer boundary of the inhomogeneous ice crystals, the computation of reflection and refraction events is the same as in the case for homogeneous hexagonal ice crystals. Since IGOM is based partly on the principles of geometric optics, very small air bubbles are not considered in the present study. The technical details and applicability of the IGOM are reported and discussed in *Yang and Liou* [1996].

If a ray is refracted into an ice crystal, the next step is to trace the refracted ray and determine if it is intersected by any air bubble within the particle. Figure 4 shows the flow-chart for reflection and refraction by internal air bubbles. For an air bubble with the particle shape given by Eq. (1), the coordinates of the incident point B, (x_b, y_b, z_b) , can be determined as follows:

$$x_b = x_a + (\hat{e} \cdot \hat{x})l, \quad (2)$$

$$y_b = y_a + (\hat{e} \cdot \hat{y})l, \quad (3)$$

$$z_b = z_a + (\hat{e} \cdot \hat{z})l, \quad (4)$$

where the coordinates (x_a, y_a, z_a) indicate the position of the first incident point, A, at the ice crystal surface, \hat{e} is a unit vector along the incident direction, \hat{x} , \hat{y} , and \hat{z} are unit vectors along the X, Y, and Z axes, respectively, and l is the distance between points A and B. Substituting Eqs. (2)-(4) into Eq. (1), we obtain

$$A_1 l^2 + A_2 l + A_3 = 0, \quad (5)$$

where

$$A_1 = r_2^2 r_3^2 (\hat{e} \cdot \hat{x})^2 + r_1^2 r_3^2 (\hat{e} \cdot \hat{y})^2 + r_1^2 r_2^2 (\hat{e} \cdot \hat{z})^2, \quad (6)$$

$$A_2 = 2r_2^2 r_3^2 (x_a - x_r)(\hat{e} \cdot \hat{x}) + 2r_1^2 r_3^2 (y_a - y_r)(\hat{e} \cdot \hat{y}) + 2r_1^2 r_2^2 (z_a - z_r)(\hat{e} \cdot \hat{z}), \quad (7)$$

$$A_3 = r_2^2 r_3^2 (x_a - x_r)^2 + r_1^2 r_3^2 (y_a - y_r)^2 + r_1^2 r_2^2 (z_a - z_r)^2 - r_1^2 r_2^2 r_3^2. \quad (8)$$

A ray will intercept an air bubble when A_1 , A_2 , and A_3 satisfy

$$A_2^2 - 4A_1A_3 > 0, \quad (9)$$

and

$$\frac{-A_2 - \sqrt{A_2^2 - 4A_1A_3}}{2A_1} > 0. \quad (10)$$

The directions of the reflected and refracted rays, \hat{e}_r and \hat{e}_t can be determined on the basis of Snell's law in the form

$$\hat{e}_r = \hat{e} - 2(\hat{e} \cdot \hat{n})\hat{n}, \quad (11)$$

$$\hat{e}_t = N_r[\hat{e} - (\hat{e} \cdot \hat{n})\hat{n} - \sqrt{N_r^2 - 1 + (\hat{e} \cdot \hat{n})^2}\hat{n}], \quad (12)$$

where N_r is the real part of the effective refractive index formulated by *Yang and Liou* [1995] and \hat{n} is the normal direction of the air-bubble surface at point B. For spheroidal air bubbles used in this study, \hat{n} can be given by

$$\hat{n}_x = \frac{x_b - x_r}{r_1^2} \bigg/ \sqrt{\left(\frac{x_b - x_r}{r_1^2}\right)^2 + \left(\frac{y_b - y_r}{r_2^2}\right)^2 + \left(\frac{z_b - z_r}{r_3^2}\right)^2}, \quad (13)$$

$$\hat{n}_y = \frac{y_b - y_r}{r_2^2} \bigg/ \sqrt{\left(\frac{x_b - x_r}{r_1^2}\right)^2 + \left(\frac{y_b - y_r}{r_2^2}\right)^2 + \left(\frac{z_b - z_r}{r_3^2}\right)^2} \quad (14)$$

$$\hat{n}_z = \frac{z_b - z_r}{r_3^2} \bigg/ \sqrt{\left(\frac{x_b - x_r}{r_1^2}\right)^2 + \left(\frac{y_b - y_r}{r_2^2}\right)^2 + \left(\frac{z_b - z_r}{r_3^2}\right)^2}. \quad (15)$$

For a ray refracted into the air bubble, the next impinging point C, (x_c, y_c, z_c) , on the air-bubble surface can be determined as follows:

$$x_c = x_b + (\hat{e}_t \cdot \hat{x})l', \quad (16)$$

$$y_c = y_b + (\hat{e}_t \cdot \hat{y})l', \quad (17)$$

$$z_c = z_b + (\hat{e}_t \cdot \hat{z})l', \quad (18)$$

where l' is the distance between points B and C. l' can be solved from Eqs. (5)-(8) by replacing l and \hat{e} by l' and \hat{e}_t , respectively.

If the conditions in Eqs. (9) and (10) are not satisfied, i.e., the incident ray does not impinge upon the air bubble centered at (x_r, y_r, z_r) , the ray-tracing procedure needs to be repeated for another air bubble if more than one air bubble is embedded in the ice crystal of interest.

3. Single-scattering properties of inhomogeneous ice crystals

Figure 5 compares the scattering phase functions for homogeneous ice crystals with their inhomogeneous ice crystal counterparts at the wavelengths (λ) of 0.65 and 2.13 μm . The refractive indices of ice at these wavelengths are $1.3080 + i1.43 \times 10^{-8}$ and $1.2673 + i5.57 \times 10^{-4}$, respectively. The ice crystals are assumed to be randomly oriented hexagonal columns and plates with aspect ratios $2a/L=80 \mu\text{m}/100 \mu\text{m}$ and $100 \mu\text{m}/43 \mu\text{m}$, respectively, where a is the radius of a cylinder that circumscribes the hexagonal ice particle and L is the length of the ice particle. Specifically, Fig. 5a shows the phase functions at $\lambda=0.65 \mu\text{m}$ for homogeneous hexagonal columns and inhomogeneous columns with the same aspect ratio. For the two inhomogeneous conditions, spherical air bubbles with radii of 16 or 34 μm are centered in the middle of ice crystals. It is then evident from Fig. 5a that the air bubbles within ice crystals can greatly affect the scattering properties of ice particles. In the homogeneous case, the 22° and 46° halo

peaks are quite pronounced, which are typical for the scattering of light by randomly oriented pristine hexagonal ice crystals. However, the magnitudes of the peaks at the scattering angles 22° and 46° are reduced if a small air bubble with a radius of $16\text{ }\mu\text{m}$ is embedded in the crystal. For ice crystals containing relatively large air bubbles with a radius of $34\text{ }\mu\text{m}$, the 22° and 46° peaks are significantly smoothed out in the scattering phase function although they are still slightly noticeable. Furthermore, the backscattering is substantially reduced in the inhomogeneous case. It should be noted that a bubble embedded in ice acts as a diverging lens and affects internal rays; however, the forward peaks are essentially unaffected by bubbles since diffraction, which depends primarily on the particle projected area, is the primary cause. Figure 5b shows the scattering phase functions for homogeneous and inhomogeneous hexagonal columns at $\lambda=2.13\text{ }\mu\text{m}$. The effect of air bubbles at the near-infrared wavelength is similar to that in the case for visible wavelengths. Figure 5c shows the scattering phase functions of hexagonal plates at $\lambda=0.65\text{ }\mu\text{m}$. In this panel, the dotted line describes the phase function for inhomogeneous ice crystals containing a spherical air bubble with a radius of $21.25\text{ }\mu\text{m}$. For the other inhomogeneous case, four air bubbles with the same size are aligned parallel to the basal faces of the plates. Comparable to the effect in the hexagonal columns, the air bubbles in hexagonal plates smooth the scattering phase function and reduce the backscatter. The phase function values at scattering angles larger than 120° are quite sensitive to the number of air bubbles in hexagonal plates. A similar effect of air bubbles on the single-scattering properties is also seen in Fig. 5d for a wavelength of $2.13\text{ }\mu\text{m}$.

250 Figure 6 shows a measure of linear polarization, $-p_{12}/p_{11}$, for ice crystals having
251 the same aspect ratios and inhomogeneities as those in Fig. 5. Figures 6a and 6b compare
252 the degrees of linear polarization between homogeneous and inhomogeneous hexagonal
253 columns. It is seen that air bubbles embedded within ice crystals can also reduce the
254 magnitude of the degree of linear polarization, particularly, in the case of large air
255 bubbles. The same effect can also be found for hexagonal plates, whose scattering phase
256 functions are shown in Figures 6c and 6d at $\lambda=0.65 \mu\text{m}$ and $\lambda=2.13 \mu\text{m}$, respectively.
257 However, unlike the scattering phase functions in Fig. 5, increasing the number of air
258 bubbles in hexagonal plates enhances the smoothing of the degree of linear polarization.

259 Figure 7 shows the phase matrices for hexagonal columns at $\lambda=0.65 \mu\text{m}$. To
260 specify the effects of the shapes of air bubbles on the single-scattering properties of ice
261 crystals, three hexagonal column ($2a/L=50 \mu\text{m} / 100 \mu\text{m}$) cases are considered: a
262 homogeneous ice crystal, an inhomogeneous ice crystal with a spherical air bubble
263 (radius= $10.0 \mu\text{m}$), and an inhomogeneous ice crystal with a volume-equivalent spheroid
264 bubble. It is evident from Fig. 7 that spheroidal air bubbles have a greater effect on the
265 phase matrix than those containing spherical air bubbles. This feature is physically
266 understandable since for the same volume, a spherical particle has the smallest cross
267 section on average among all solid particles, and an incident ray has a smaller chance to
268 be intercepted by spherical air bubbles than their counterparts with other shapes. In
269 addition to the phase function and degree of linear polarization, the other elements of the
270 phase matrix are also sensitive to the presence of air bubbles.

271 To further illustrate the effect of air bubbles on the single-scattering properties of
272 ice crystals, Fig. 8 shows the asymmetry factor as a function of the volume of the air

bubbles at $\lambda=0.65\ \mu\text{m}$ and $\lambda=2.13\ \mu\text{m}$. The aspect ratio of ice crystals is $2a/L=10\ \mu\text{m}/50\ \mu\text{m}$. Spherical air bubbles are located at the center of the ice crystals where the radii r_1 and r_2 in Eq. (1) are the same. The relative volume of the air bubble, V_b/V , can be specified in terms of the radii, where V_b and V are the volumes of the air bubbles and ice crystals, respectively. It is seen from Fig. 8 that the asymmetry factor decreases at both visible and near-infrared wavelengths when small air bubbles are included. The asymmetry factor reaches its minimum value with increasing V_b/V and may increase when back-scattering is significantly reduced by considering extremely large air bubbles. These features are found to be applicable to all the inhomogeneous ice crystals containing one air bubble shown in Fig. 2.

4. Effect of inhomogeneous ice crystals on ice cloud retrieval

The single-scattering properties of ice crystals are fundamental to the development of the lookup tables required for satellite-based ice cloud retrieval algorithms. At present, substantial uncertainties exist in ice cloud property retrievals due to inadequate representation of complex ice crystal morphologies and, consequently, inaccurate knowledge about their single-scattering properties. Inhomogeneous ice crystal morphology is one of the least understood aspects in defining realistic ice crystal geometries. Additional in situ measurements are required to quantify the occurrence frequency of air bubbles within ice crystals and their importance in radiative transfer simulations and remote sensing applications.

To study the effect of inhomogeneous ice crystals on retrieving ice cloud properties, aspect ratios of ice crystals as well as particle size distributions are required.

296 In this sensitivity study, an aspect ratio of $2a/L=0.2$ is used for all ice crystals, although it
 297 may not correspond well to observations [Ono, 1969]. Realistic aspect ratios are needed
 298 in future studies. Furthermore, small ($r_1=0.45a$, $r_2=0.45a$, and $r_3=0.2L$) and relatively
 299 large ($r_1=0.85a$, $r_2=0.85a$, and $r_3=0.2L$) air bubbles are defined at the center of each
 300 inhomogeneous ice crystal. The size distribution of ice crystals is assumed to obey a
 301 Gamma distribution given by

$$302 \quad n(L) = N_0 L^\mu \exp\left(-\frac{b + \mu + 0.67}{L_m} L\right), \quad (19)$$

303 where N_0 is the intercept, μ is assumed to be 2 in this study, and L_m is the median of the
 304 distribution of L . The parameter b is taken to be 2.2. The effective particle size for a
 305 given size distribution is defined as follows [Foot, 1988]:

$$306 \quad r_e = \frac{3 \int_{L_{\min}}^{L_{\max}} V(L) n(L) dL}{4 \int_{L_{\min}}^{L_{\max}} A(L) n(L) dL}, \quad (20)$$

307 where V is particle volume, and A is projected area.

308 The ice cloud bi-directional reflectances are computed using the Discrete
 309 Ordinates Radiative Transfer (DISORT) model [Stamnes *et al.*, 1988] for $\lambda = 0.65$ and
 310 $2.13 \mu\text{m}$ at various incident-scattering configurations. The visible optical thickness at $\lambda =$
 311 $0.65 \mu\text{m}$ serves as the reference optical thickness in this study. The optical thickness for a
 312 given wavelength is related to the visible optical thickness via

$$313 \quad \tau = \frac{\tau_{\text{vis}} Q}{Q_{\text{vis}}}, \quad (21)$$

314 where Q and Q_{vis} are the extinction efficiencies for $\lambda=2.13$ and $0.65 \mu\text{m}$, respectively.

315 Figure 9a shows the comparison of the lookup tables computed for the solid
 316 homogeneous ice crystals and the inhomogeneous ice crystals containing small air

bubbles ($r_1 = r_2 = 0.45a$, and $r_3 = 0.2L$). It is seen that the inhomogeneous ice crystals reflect slightly more than the homogeneous ice crystals at $\lambda = 0.65 \mu\text{m}$ whereas the bidirectional reflectances for the inhomogeneous ice crystals are significantly larger than those for the homogeneous particles at $\lambda = 2.13 \mu\text{m}$. Figure 9b is the same as Fig. 9a except that each inhomogeneous ice crystal in Fig. 9b contains larger air bubbles with radii of $r_1 = r_2 = 0.85a$, and $r_3 = 0.2L$. It is then evident that the bidirectional reflectances at $\lambda = 0.65 \mu\text{m}$ are slightly sensitive to the air bubble size. However, large air bubbles in the ice crystals can significantly increase the reflectances at $\lambda = 2.13 \mu\text{m}$.

The left and right panels in the top of Fig. 10 show a MODIS granule image over the south Pacific Ocean on April 17, 2007 and the cloud mask from the operational MODIS cloud product, respectively. The middle and lower panels of Fig. 10 show the retrieved cloud properties for the pixels that have been identified as covered by ice clouds. Specifically, the middle panel on the left compares the retrieved ice cloud optical thickness from homogeneous and inhomogeneous ice crystals. For the latter, small air bubbles ($r_1 = r_2 = 0.45a$, and $r_3 = 0.2L$) are embedded. The middle panel on the right is the same as the left panel except that the inhomogeneous ice crystals have larger air bubbles ($r_1 = r_2 = 0.85a$, and $r_3 = 0.2L$). It is then evident that the cloud optical thicknesses are slightly reduced by using inhomogeneous ice crystal models in ice cloud property retrievals. These results are consistent with Fig. 9 where the inhomogeneous ice crystals reflect more than homogeneous ice crystals at $\lambda = 0.65 \mu\text{m}$. The increase in the sizes of air bubbles can further reduce the optical thickness as evident from the comparison of the two middle panels in Fig. 10. Using inhomogeneous ice crystals in ice cloud models may also significantly increase the retrieved ice cloud effective particle sizes, as evident from

the lower panels in Fig. 10. Moreover, this effect becomes more significant as sizes of the air bubbles increase.

Figures 9 and 10 describe the sensitivities of ice cloud reflectance and cloud property retrievals to the optical properties of inhomogeneous ice crystals on the basis of the bi-spectral method developed by *Nakajima and King* [1990]. In this study, the same particle volumes and size distributions are employed for both homogeneous and inhomogeneous ice crystals. However, air bubbles within ice crystals decrease the volume of ice and therefore decrease the effective particle size of ice crystals in the ice cloud. Figure 11 shows the variations of the effective particle size versus the volume of the air bubbles within an ice crystal. It is seen that the effective particle size of ice clouds can be reduced by more than 50%, depending on the shapes and sizes of the air bubbles within ice crystals. Thus, the increased effective particle size resulting from a retrieval employing inhomogeneous ice crystals in Fig. 10 can be partly compensated for if the volumes of the air bubbles are subtracted from the particle volumes.

5. Summary

This study reports on the single-scattering properties of inhomogeneous ice crystals whose geometries are defined on the basis of the observations made by *Tape* [1994] at the South Pole. Unlike the spherical air bubbles with random locations in the IHM model previously developed by *Labonnote et al.* [2001], in the present study, a few spherical or spheroidal air bubbles are defined within hexagonal ice crystals. The sensitivity of single-scattering properties to inhomogeneous ice crystals has been examined. It is found that the single-scattering phase function is substantially smoothed

out and the 22° and 46° halos are reduced if air bubbles are included in the ice crystals. These features have been previously reported [Labonnote *et al.*, 2001; Macke *et al.*, 1996]. The phase function smoothing can become more pronounced by increasing the number of air bubbles, enlarging the air bubble, changing the air bubbles' shapes from spheres to spheroids, or moving them from the sides to the center of an ice crystal. The peaks of the degree of linear polarization can also be reduced by considering inhomogeneous ice crystals. Moreover, the asymmetry factors of inhomogeneous ice crystals may decrease to a minimum value and increase as the relative volume of the air bubbles increases.

Furthermore, a lookup library of bidirectional reflectances has been developed for both homogeneous and inhomogeneous ice cloud models at $\lambda = 0.65$ and $2.13 \mu\text{m}$. We have shown that using inhomogeneous ice cloud models can increase the bidirectional reflectances at those two wavelengths. Therefore, the retrieved ice cloud optical thicknesses are slightly reduced whereas the retrieved ice cloud effective particle sizes can be significantly increased by including air bubbles in ice crystals, particularly, in the case of large air bubbles. This effect is similar to that found when surface roughness is included in the computations of ice crystal single-scattering properties [Yang *et al.*, 2008a,b], except that the presence of air bubbles in the crystals reduces the overall ice water content compared to a solid crystal with roughened surfaces. These results represent another important step in the effort to develop realistic ice crystal optical properties for use in retrieving ice cloud properties from satellite imagery and representing them in numerical weather and climate models. The results appear to be in the right direction for decreasing the biases in retrieved ice cloud optical properties, .e.g.,

Min et al. [2004]. Additional study will be needed, however, to determine if the optical properties of spheroidal bubbles, either alone or in combination with those for other ice crystal formulations, can provide a more accurate representation of actual ice crystal reflectance behavior.

Acknowledgements

This research is supported by a National Science Foundation (NSF) grant (ATM-0239605) managed by Dr. Bradley Smull and by a NASA grant (NNL06AA23G). George W. Kattawar's research is also supported by the Office of Naval Research under contract N00014-06-1-0069. Patrick Minnis is supported through the NASA Radiation Sciences Program and the NASA Clouds and the Earth's Radiant Energy System Project.

References

- Baran, A. J. (2004), On the scattering and absorption properties of cirrus cloud, *J. Quant. Spectrosc. Radiat. Transfer*, 89, 17-36.
- Baran, A. J. and L. C. Labonnote (2006), On the reflection and polarization properties of ice cloud, *J. Quant. Spectrosc. Radiat. Transfer*, 100, 41-54.
- Baran, A. J. and L. C. Labonnote (2007), A self-consistent scattering model for cirrus. I: The solar region, *Q. J. R. Meteorol. Soc.*, 133, 1899-1912.
- Baum, B. A., P. Yang, A. J. Heymsfield, S. Platnick, M. D. King, Y. X. Hu, and S. M. Bedka (2005a), Bulk Scattering Properties for the Remote Sensing of Ice Clouds. II: Narrowband Models. *J. Appl. Meteor.* 44, 1896-1911.
- Baum, B. A., A. J. Heymsfield, P. Yang, and S. M. Bedka (2005b), Bulk Scattering Properties for the Remote Sensing of Ice Clouds. I: Microphysical Data and Models. *J. Appl. Meteor.* 44, 1885-1895.
- Borovoi, A. G., and I. A. Grishin (2003), Scattering matrices for large ice crystal particles, *J. Opt. Soc. Am. A.*, 20, 2071-2080.
- Carte, A. E. (1961), Air bubbles in ice, *Proc. Phys. Soc.*, 77, 757-768.
- Foot, J. S. (1988), Some observations of the optical properties of clouds. II: Cirrus, *Q. J. R. Meteorol. Soc.*, 114, 145-169.
- Hallett, J. (1964), Experimental studies of the crystallization of supercooled water, *J. Atmos. Sci.*, 21, 671-682.
- Hess M., R. B. A. Koelemeijer, and P. Stammes (1998), Scattering matrices of imperfect hexagonal ice crystals. *J. Quant. Spectrosc. Radiat. Transfer*, 60, 301-308.

425 Hess M., and M. Wiegner (1994), COP: a data library of optical properties of hexagonal
 426 ice crystals, *Appl. Opt.*, 33, 7740-7746.
 427 Iaquinta, J., H. Isaka, and P. Personne (1995), Scattering phase function of bullet rosette
 428 ice crystals, *J. Atmos. Sci.*, 52, 1401-1413.
 429 Knap, W. H., L. C. Labonnote, G. Brogniez, and P. Stammes (2005), Modeling total and
 430 polarized reflectances of ice clouds: evaluation by means of POLDER and ATSR-
 431 2 measurements, *Appl. Opt.*, 44, 4060-4073.
 432 Korolev, A. V., G. A. Isaac, and J. Hallett (1999), Ice particle habits in Arctic clouds,
 433 *Geophys. Res. L.*, 26, 1299-1302.
 434 Labonnote, L. C., G. Brogniez, J. C. Buriez, and M. Doutriaux-Boucher (2001), Polarized
 435 light scattering by inhomogeneous hexagonal monocrystals: validation with
 436 ADEOS-POLDER measurements, *J. Geophys. Res.*, 106, 12139-12155.
 437 Liou, K. N. (1972), Light scattering by ice clouds in the visible and infrared: a theoretical
 438 study, *J. Atmos. Sci.*, 29, 524-536.
 439 Liou, K. N. (1986), Influence of cirrus clouds on weather and climate processes: A global
 440 perspective, *Mon. Wea. Rev.*, 114, 1167-1199.
 441 Mace, G. G., Y. Zhang, S. Platnick, M. D. King, P. Minnis, and P. Yang (2005),
 442 Evaluation of cirrus cloud properties from MODIS radiances using cloud
 443 properties derived from ground-based data collected at the ARM SGP site, *J.*
 444 *Appl. Meteorol.*, 44, 221-240.
 445 Macke, A. (1993), Scattering of light by polyhedral ice crystals, *Appl. Opt.*, 32, 2780-
 446 2788.

447 Macke, A., M. I. Mishchenko, and B. Cairns (1996a), The influence of inclusions on light
 448 scattering by large ice particles, *J. Geophys. Res.*, 101, 23311-23316.

449 Macke, A. J. Mueller, and E. Raschke (1996b), Single scattering properties of
 450 atmospheric ice crystal, *J. Atmos. Sci.*, 53, 2813-2825.

451 McFarquhar, G. M. and A. J. Heymsfield (1996), Microphysical characteristics of three
 452 Anvils sampled during the Central Equatorial Experiment, *J. Atmos. Sci.*, 53,
 453 2401-2423.

454 Min, Q. P. Minnis, and M. M. Khaiyer (2004), Comparison of cirrus optical depths from
 455 GOES-8 and surface measurements, *J. Geophys. Res.*, 109, D20119,
 456 10.1029/2003JD004390.

457 Minnis, P., D. P. Garber, D. F. Young, R. F. Arduini, and Y. Takano (1998),
 458 Parameterization of reflectance and effective emittance for satellite remote
 459 sensing of cloud properties, *J. Atmos. Sci.*, 55, 3313-3339.

460 Minnis, P., P. W. Heck, and D. F. Young (1993), Inference of cirrus cloud properties
 461 using satellite-observed visible and infrared radiances, Part II: Verification of
 462 theoretical cirrus radiative properties, *J. Atmos. Sci.*, 50, 1305-1322.

463 Mishchenko, M. I., J. W. Hovenier and L. D. Travis (2000), *Light scattering by*
 464 *nonspherical particles*, Academic press, San Diego, San Francisco, New York,
 465 Boston, London, Sydney, Tokyo.

466 Muinonen, K. (1989), Scattering of light by crystals: a modified Kirchhoff
 467 approximation, *Appl. Opt.*, 28, 3044-3050.

468 Nakajima T. and M. D. King (1990), Determination of the optical thickness and effective
 469 particle radius of clouds from reflected solar radiation measurements. Part I:
 470 Theory, *J. Atmos. Sci.*, 47, 1878-1893.

471 Ono, A. (1969), The shape and riming properties of ice crystals in natural clouds, *J.*
 472 *Atmos. Sci.*, 26, 138-147.

473 Ramanathan, V., E. J. Pitcher, R. C. Malone, and M. L. Blackmon (1983), The response
 474 of a general circulation model to refinements in radiative processes, *J. Atmos.*
 475 *Sci.*, 40, 605-630.

476 Schmitt, C. G., J. Iaquinta, and A. J. Heymsfield (2006), The asymmetry parameter of
 477 cirrus clouds composed of hollow bullet rosette-shaped ice crystals from ray-
 478 tracing calculations. *J. Appl. Meteor. and Climat.*, 45, 973–981.

479 Stamnes, K., S. C. Tsay, W. Wiscombe, and K. Jayaweera (1988), Numerically stable
 480 algorithm for discrete-ordinate-method radiative transfer in multiple scattering
 481 and emitting layered media. *Appl. Opt.*, 27, 2502-2509.

482 Takano, Y and K. N. Liou (1989), Solar radiative transfer in cirrus clouds. Part I: single-
 483 scattering and optical properties of hexagonal ice crystals, *J. Atmos. Sci.*, 46, 3-19.

484 Takano, Y. and K.N. Liou (1995), Radiative transfer in cirrus clouds. III. Light scattering
 485 by irregular ice crystals, *J. Atmos. Sci.*, 52, 818-837.

486 Tape, W. (1983), Some ice crystals that made halos, *J. Opt. Soc. Am.*, 73, 1641-1645.

487 Tape, W. (1994), *Atmospheric halos*, American Geophysical Union, Washington, D. C.,
 488 USA.

489 Um, J., and G. M. McFarquhar (2007), Single-Scattering Properties of Aggregates of
 490 Bullet Rosettes in Cirrus, *J. Appl. Meteor. and Climatology*, 46, 757–775.

491 Yang P., G. Hong, G. W. Kattawar, P. Minnis and Y. X. Hu (2008a), Uncertainties
 492 associated with the surface texture of ice particles in satellite-based retrieval of
 493 cirrus clouds: Part II. Effect of particle surface roughness on retrieved cloud
 494 optical thickness and effective particle size, *Geo. Remote. Sens.*, 46, 1948-1957.

495 Yang, P., G. W. Kattawar, G. Hong, P. Minnis and Y. X. Hu (2008b), Uncertainties
 496 associated with the surface texture of ice particles in satellite-based retrieval of
 497 cirrus clouds: Part I. Single-scattering properties of ice crystals with surface
 498 roughness, *Geo. Remote. Sens.*, 46, 1940-1947.

499 Yang, P., and K. N. Liou (1995), Light scattering by hexagonal ice crystals: comparison
 500 of finite-difference time domain and geometric optics models, *J. Opt. Soc. Am.*,
 501 A12, 162-176.

502 Yang, P., and K. N. Liou (1996), Geometric-Optics-integral-equation method for light
 503 scattering by nonspherical ice crystals. *Appl. Opt.*, 35, 6568–6584.

504 Yang, P., and K. N. Liou (1998), Single-scattering properties of complex ice crystals in
 505 terrestrial atmosphere, *Contr. Atmos. Phys.*, 71, 223-248.

506 Yang, P., K. N. Liou, M. I. Mishchenko, and B. C. Gao (2000), An efficient finite-
 507 difference time domain scheme for light scattering by dielectric particles:
 508 application to aerosols, *Appl. Opt.*, 39, 3727-3737.

509 Yang, P., Z. B. Zhang, G. W. Kattawar, S. G. Warren, B. A. Baum, H. L. Huang, Y. X.
 510 Hu, D. Winker, and J. Iaquinta (2008c), Effect of cavities on the optical properties
 511 of bullet rosettes: Implications for active and passive remote sensing of ice cloud
 512 properties, *J. Appl. Meteorol. Climatol.*, 47, 2311-2330.

513
 514

514 **Figure Captions**

515 Fig. 1. Inhomogeneous ice crystals sampled by Walter Tape [Tape, 1994] at the South
516 Pole, on January 19, 1985 (left) and on January 17, 1986 (right).

517 Fig. 2. The geometries of inhomogeneous ice crystals.

518 Fig. 3 Geometry of a hexagonal ice crystal with an air bubble inside.

519 Fig. 4. Schematic flow-chart for reflection and refraction by internal air bubbles.

520 Fig. 5. Scattering phase functions for homogeneous and inhomogeneous ice crystals at
521 $\lambda=0.65 \mu\text{m}$ (panels a and c) and $2.13 \mu\text{m}$ (panels b and d).

522 Fig. 6. Degrees of linear polarization for homogeneous and inhomogeneous ice crystals at
523 $\lambda=0.65 \mu\text{m}$ (panels a and c) and $2.13 \mu\text{m}$ (panels b and d). The ice crystals' sizes
524 and morphologies in this figure are the same as those in Fig. 5.

525 Fig. 7. Scattering phase matrixes for homogeneous and inhomogeneous ice crystals at
526 $\lambda=0.65 \mu\text{m}$.

527 Fig. 8. Asymmetry factors for inhomogeneous ice crystals at $\lambda=0.65 \mu\text{m}$ (left) and 2.13
528 μm (right).

529 Fig. 9. Lookup tables using 0.65 and $2.13 \mu\text{m}$ reflectances for homogeneous and
530 inhomogeneous cloud models. $\mu_0=0.65$, $\mu=1.0$ and $\varphi - \varphi_0 = 0^\circ$.

531 Fig. 10. MODIS granule image (RGB=band 4:3:1) from Terra on April 17, 2007, and
532 MODIS cloud mask (upper panels). The comparisons of retrieved ice cloud
533 optical thicknesses from homogeneous and inhomogeneous ice crystals (middle
534 panels). The comparisons of retrieved ice cloud effective particle sizes from
535 homogeneous and inhomogeneous ice crystals (lower panels).

536 Fig. 11. Effective particle sizes for inhomogeneous ice crystals.

537

538

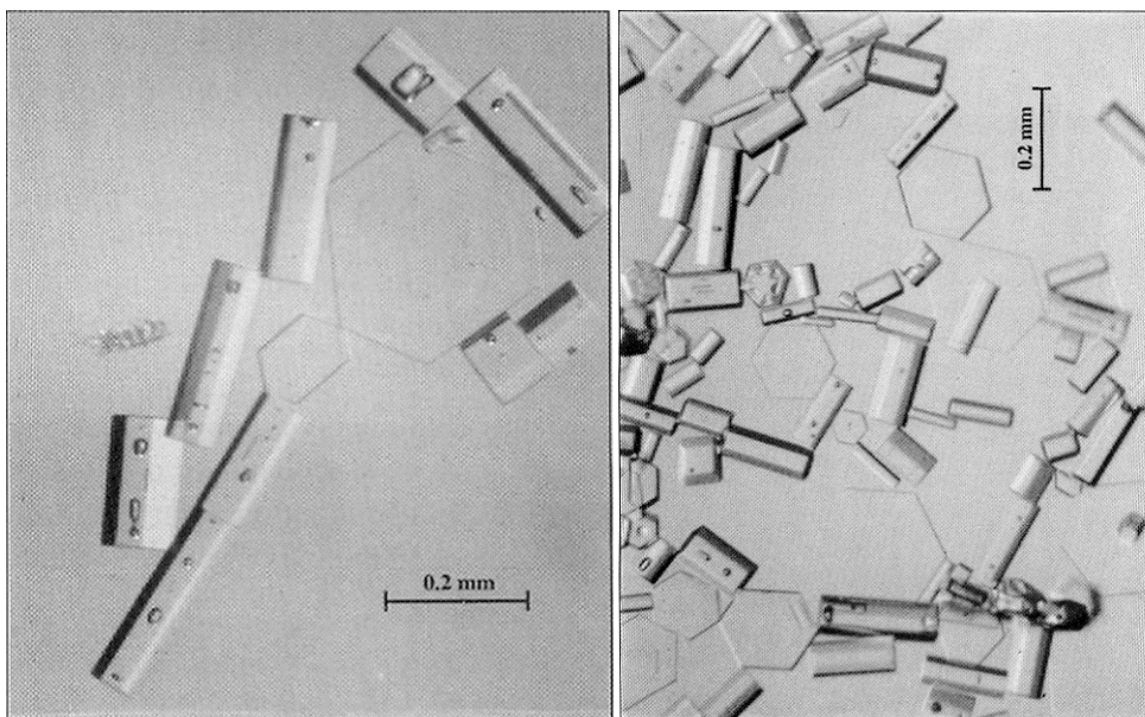
539

540

541

542

543



544

545 Fig. 1. Inhomogeneous ice crystals sampled by Walter Tape [Tape, 1994] at the South
546 Pole, on January 19, 1985 (left) and on January 17, 1986 (right).

547

548

549

550

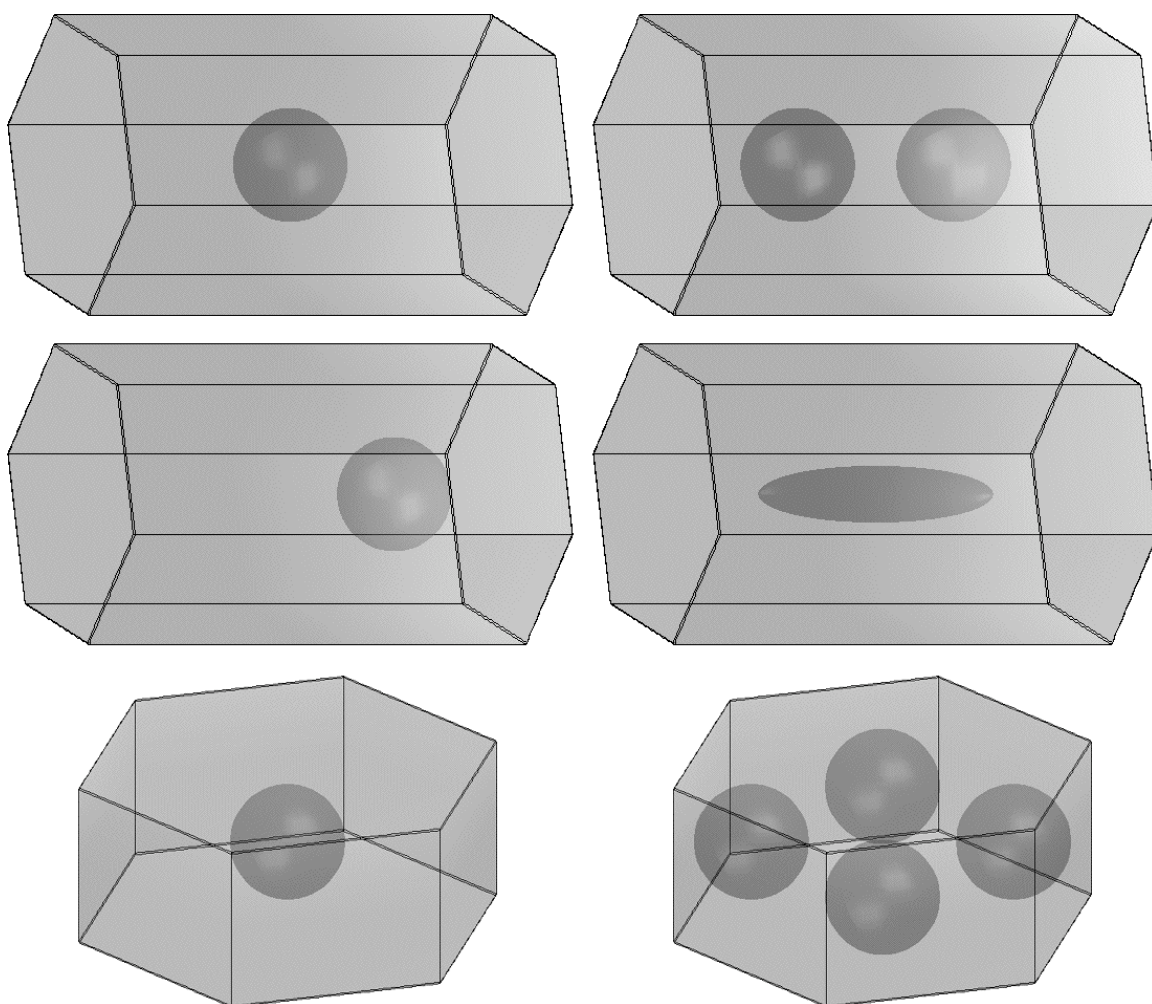
551

552

553

554

555



556

557

558 Fig. 2. The geometries of inhomogeneous ice crystals.

559

560

561

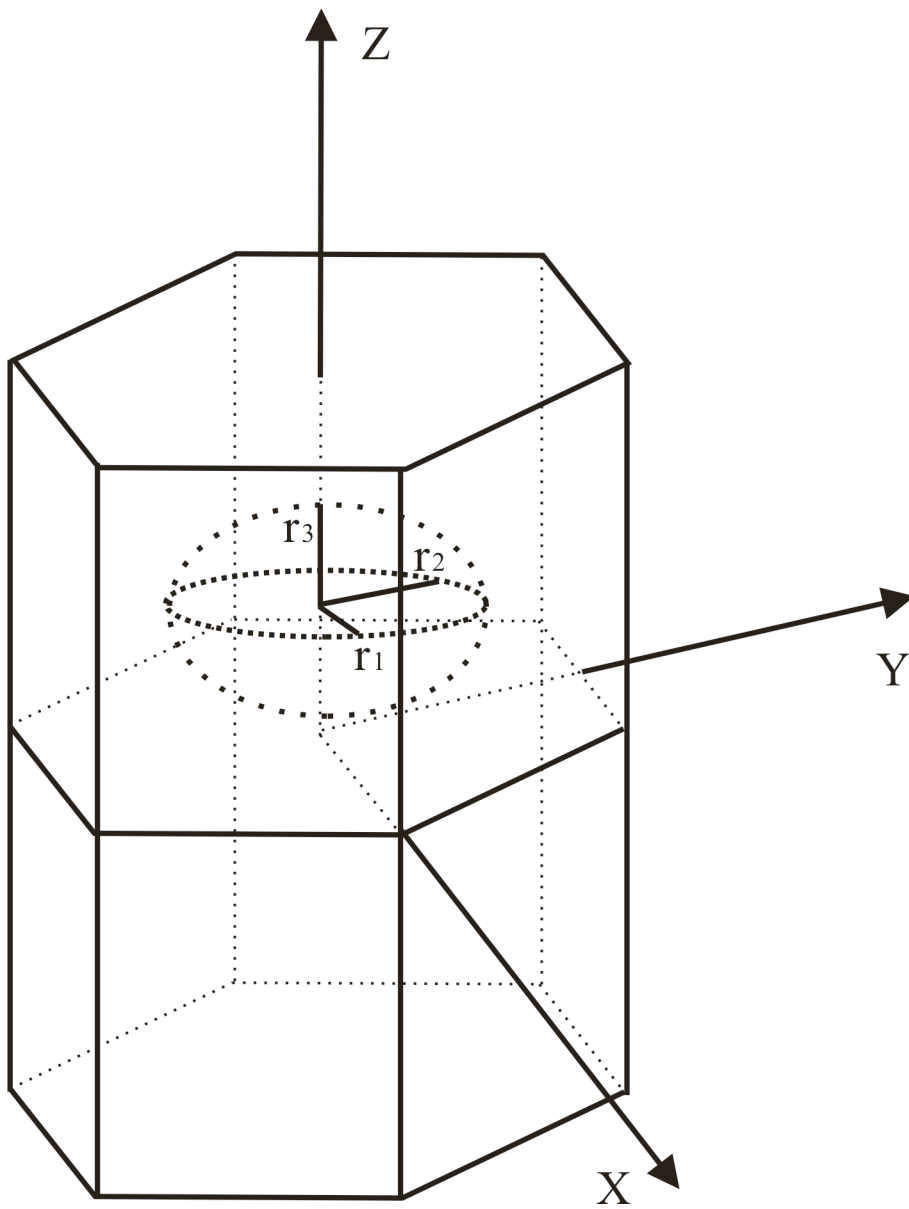
562

563

564

565

566



567

568 Fig. 3 Geometry of a hexagonal ice crystal with an air bubble inside.

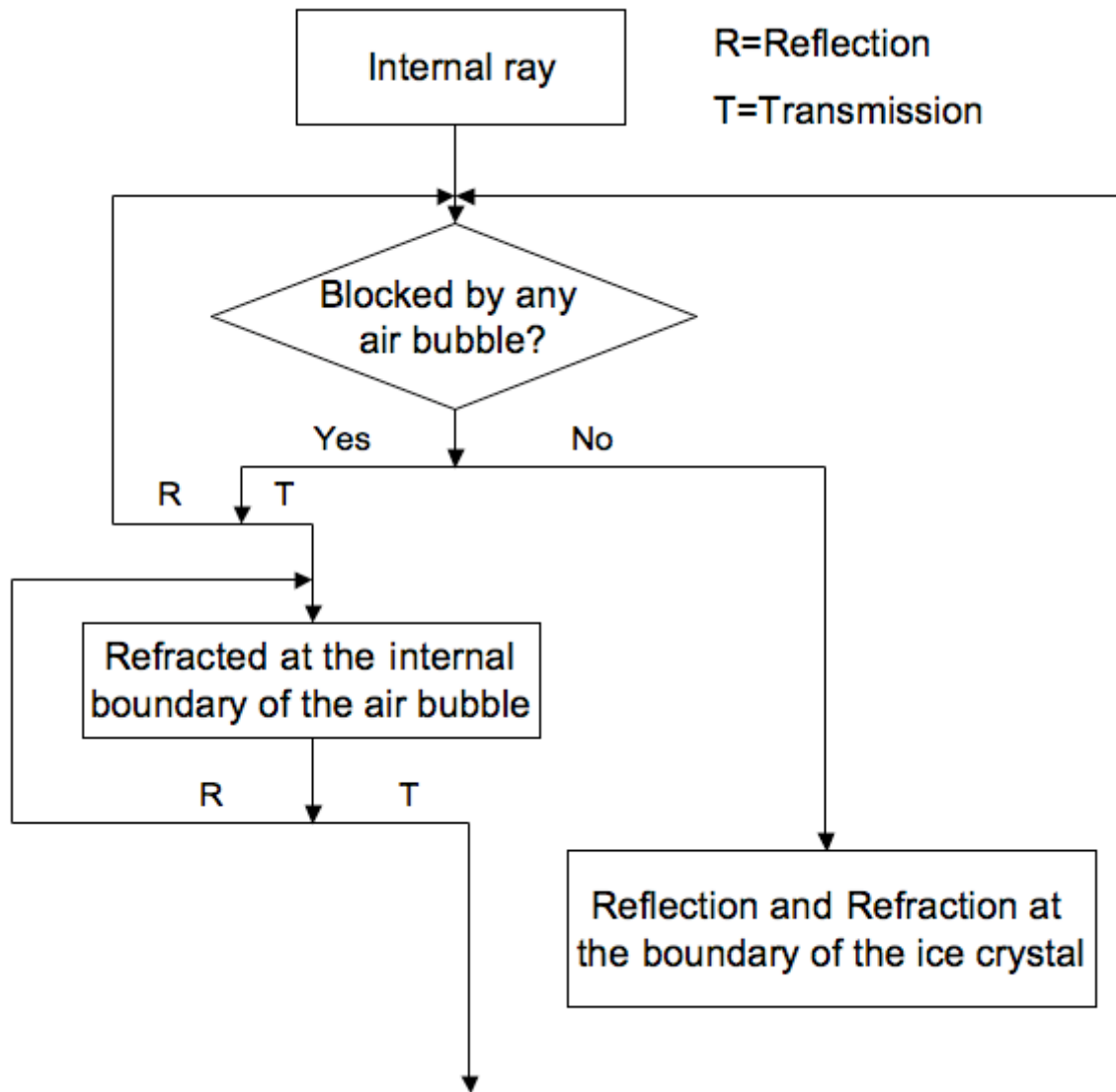
569

570

571

572

573

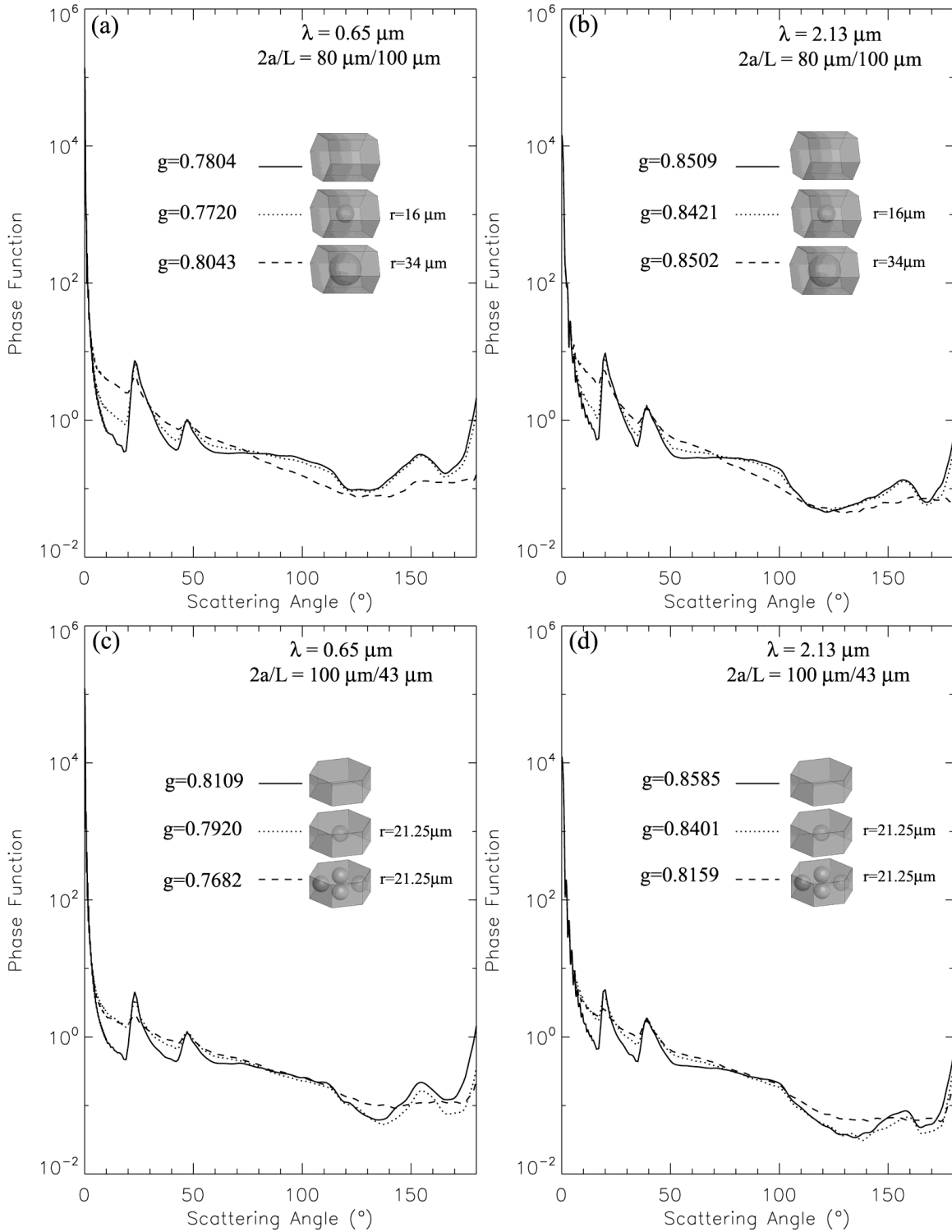


574

575

576 Fig. 4. Schematic flow-chart for reflection and refraction by internal air bubbles.

577



578

579 Fig. 5. Scattering phase functions for homogeneous and inhomogeneous ice crystals at

580 $\lambda=0.65 \mu\text{m}$ (panels a and c) and $2.13 \mu\text{m}$ (panels b and d).

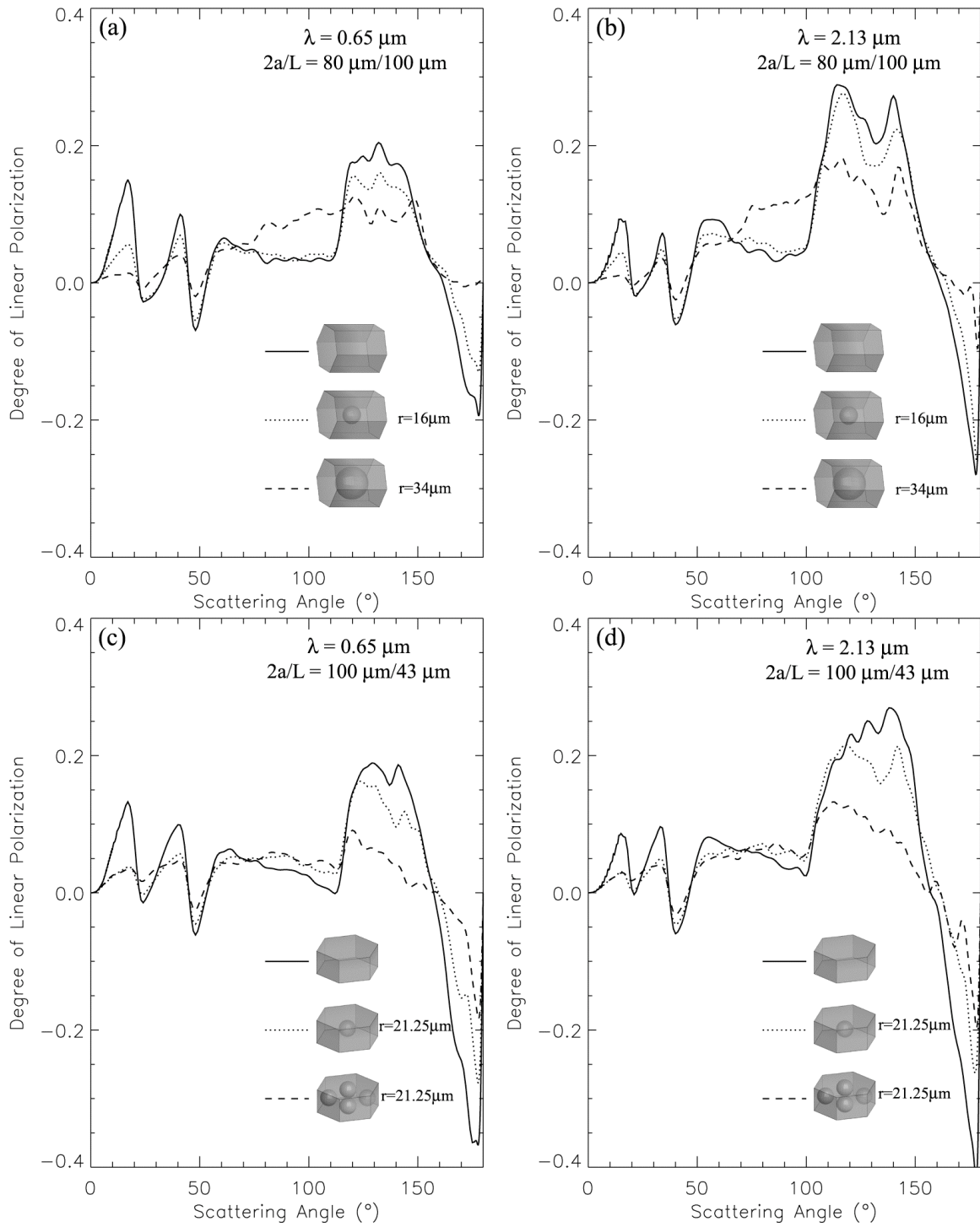


Fig. 6. Degrees of linear polarization for homogeneous and inhomogeneous ice crystals at $\lambda=0.65 \mu\text{m}$ (panels a and c) and $2.13 \mu\text{m}$ (panels b and d). The ice crystals' sizes and morphologies in this figure are the same as those in Fig. 5.

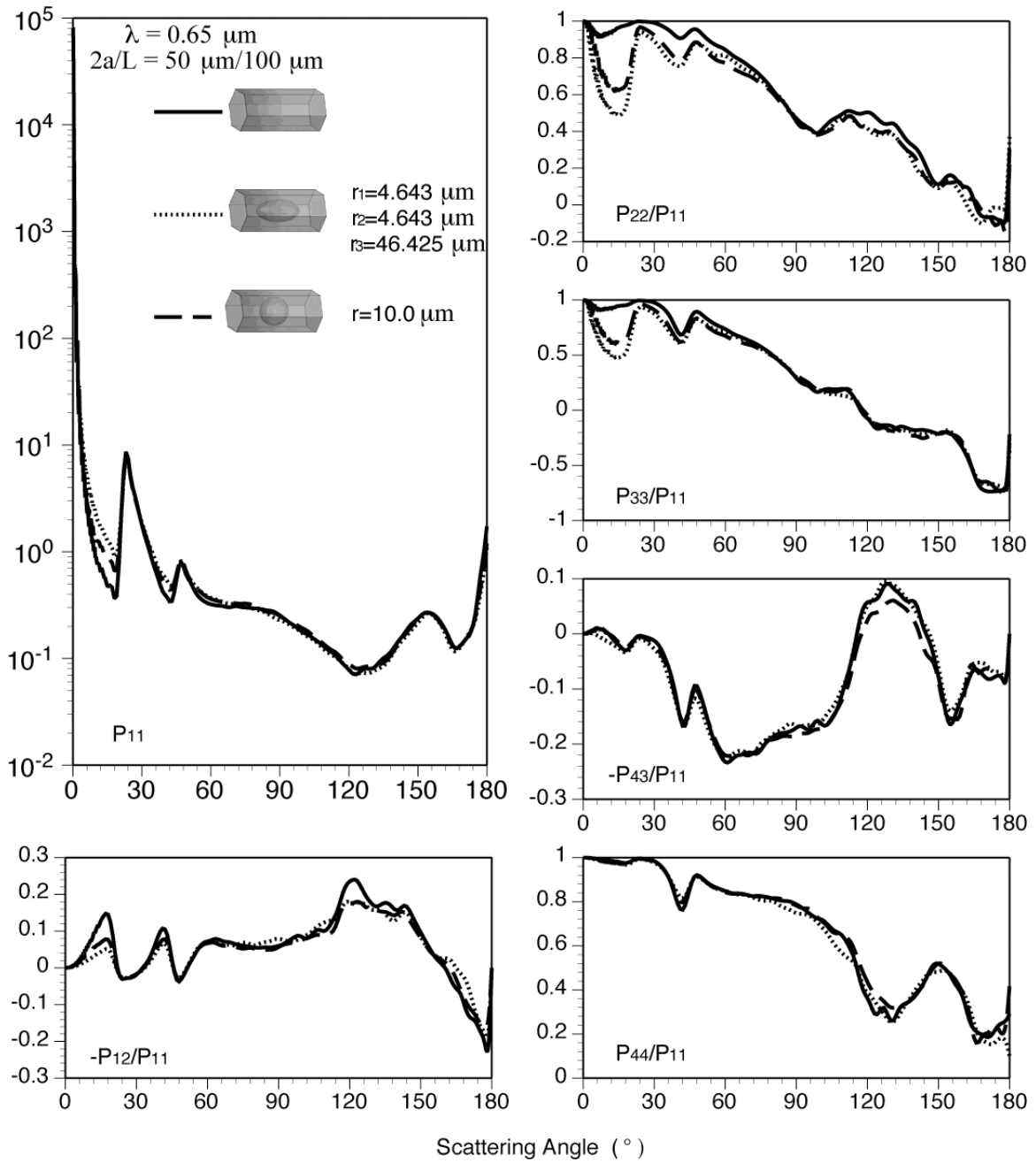


Fig. 7. Scattering phase matrixes for homogeneous and inhomogeneous ice crystals at $\lambda=0.65 \text{ } \mu\text{m}$.

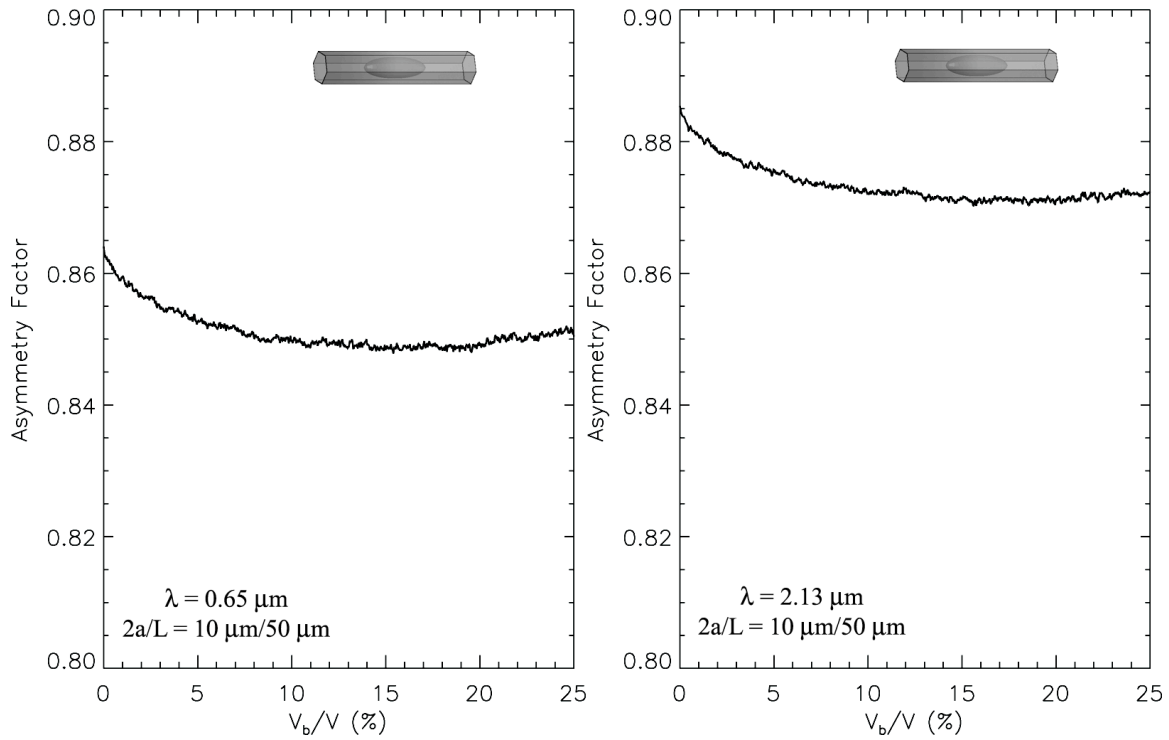


Fig. 8. Asymmetry factors for inhomogeneous ice crystals at $\lambda=0.65 \mu\text{m}$ (left) and $2.13 \mu\text{m}$ (right).

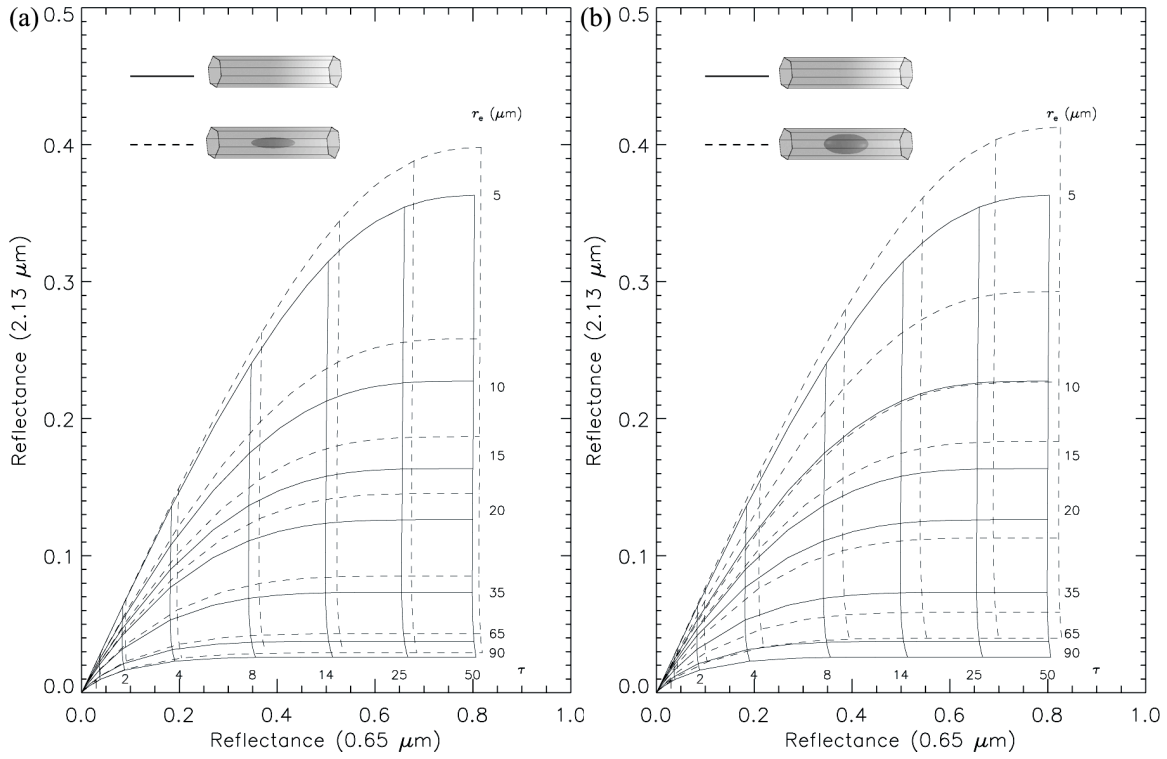


Fig. 9. Lookup tables using 0.65 and 2.13 μm reflectances for homogeneous and inhomogeneous cloud models. $\mu_0=0.65$, $\mu=1.0$ and $\varphi - \varphi_0 = 0^\circ$.

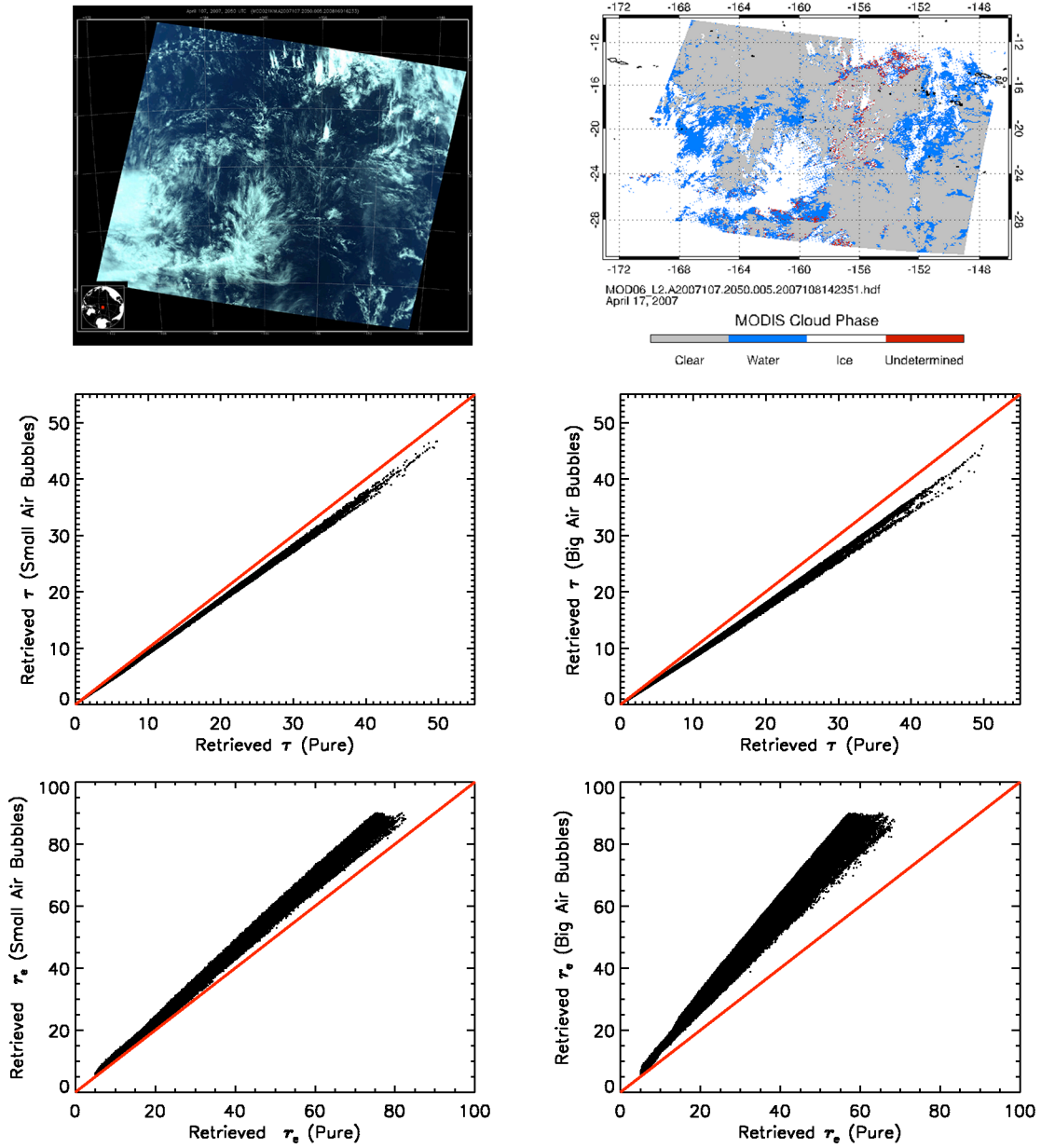


Fig. 10. MODIS granule image (RGB=band 4:3:1) from Terra on April 17, 2007, and MODIS cloud mask (upper panels). The comparisons of retrieved ice cloud optical thicknesses from homogeneous and inhomogeneous ice crystals (middle panels). The comparisons of retrieved ice cloud effective particle sizes from homogeneous and inhomogeneous ice crystals (lower panels).

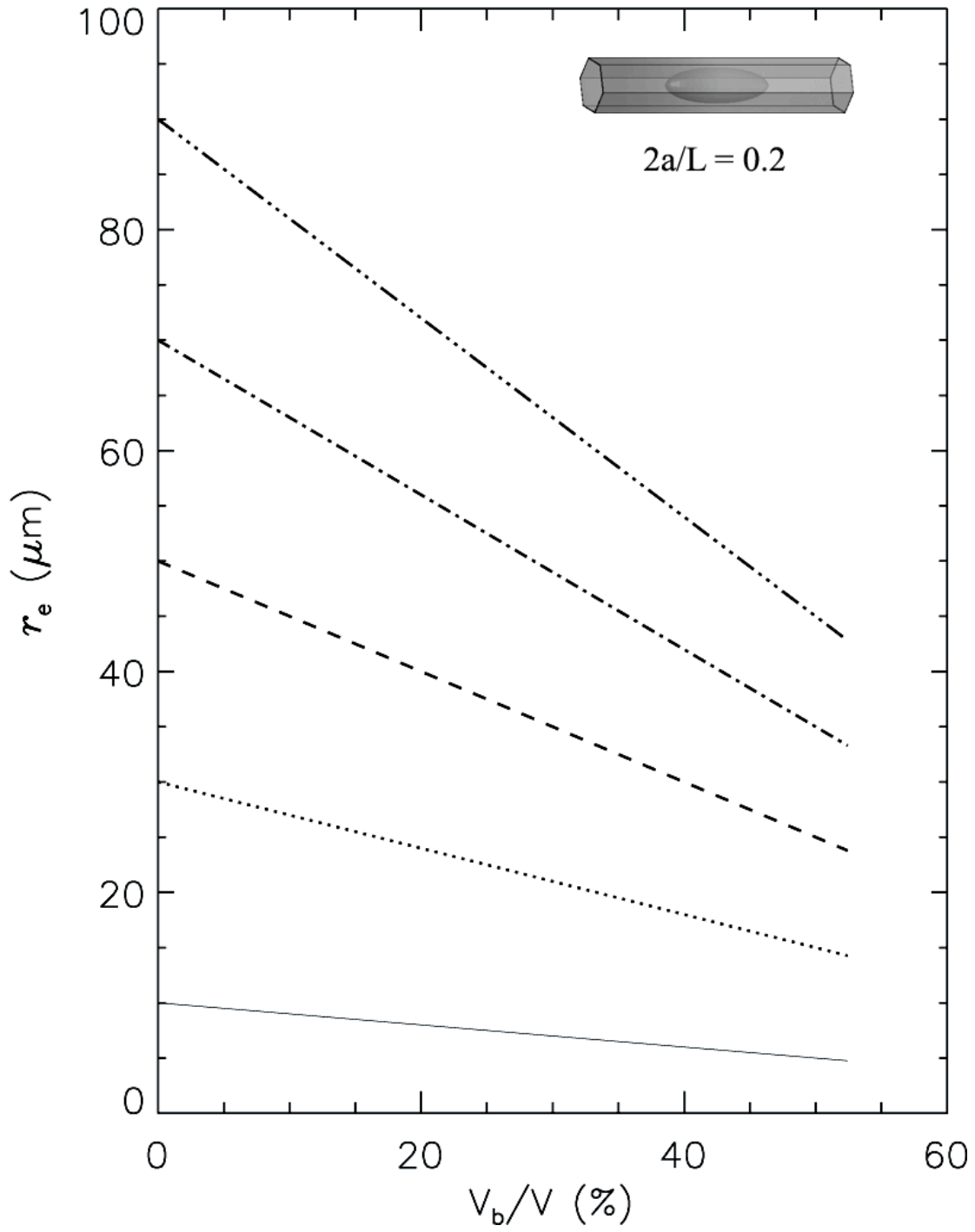


Fig. 11. Effective particle sizes for inhomogeneous ice crystals.